IP_3-mediated gating mechanism of the IP_3 receptor revealed by mutagenesis and X-ray crystallography

Kozo Hamada[a], Hideyuki Miyatake[b], Akiko Terauchi[a], and Katsuhiko Mikoshiba[a,1]

[a]Laboratory for Developmental Neurobiology, Brain Science Institute, RIKEN, Saitama 351-0198, Japan; and [b]Nano Medical Engineering Laboratory, RIKEN, Saitama 351–0198, Japan

Edited by Solomon H. Snyder, Johns Hopkins University School of Medicine, Baltimore, MD, and approved March 24, 2017 (received for review January 26, 2017)

The inositol 1,4,5-trisphosphate (IP_3) receptor (IP_3R) is an IP_3-gated ion channel that releases calcium ions (Ca^{2+}) from the endoplasmic reticulum. The IP_3-binding sites in the large cytosolic domain are distant from the Ca^{2+} conducting pore, and the allosteric mechanism of how IP_3 opens the Ca^{2+} channel remains elusive. Here, we identify a long-range gating mechanism uncovered by channel mutagenesis and X-ray crystallography of the large cytosolic domain of mouse type 1 IP_3R in the absence and presence of IP_3. Analyses of two distinct space group crystals uncovered an IP_3-dependent global translocation of the curvature α-helical domain interfacing with the cytosolic and channel domains. Mutagenesis of the IP_3R channel revealed an essential role of a leaflet structure in the α-helical domain. These results suggest that the curvature α-helical domain relays IP_3-controlled global conformational dynamics to the channel through the leaflet, conferring long-range allosteric coupling from IP_3 binding to the Ca^{2+} channel.

allosteric regulation | calcium channel | IP_3 receptor | X-ray crystallography | gating mechanism

A large variety of extracellular signals bind to evolutionarily diverse plasma membrane receptors and converge into the formation of intracellular chemical signals acting on only a few types of intracellular transmembrane receptors. One of these major intracellular receptors is the inositol 1,4,5-trisphosphate (IP_3) receptor (IP_3R) in the endoplasmic reticulum (ER), which releases calcium ions (Ca^{2+}) from the ER into the cytosol in response to the second messenger IP_3 cleaved from phosphatidylinositol 4,5-bisphosphates on G protein-coupled receptor stimulation (1–3). A full-length IP_3R gene has been cloned from mouse Purkinje neurons (4), and three isoforms have been identified (2). The brain-dominant type 1 IP_3R (IP_3R1) regulates long-term potentiation/depression (2, 5–7) and spinogenesis (8), is genetically causative for spinocerebellar ataxia 15 (9, 10) and is implicated in the etiology of Alzheimer's disease (11, 12) and Huntington's disease (13, 14). Despite these important roles of IP_3R in normal and disease conditions, the basic gating mechanism of how IP_3 opens the Ca^{2+} channel remains elusive.

IP_3R genes encode a large cytosolic domain and a small Ca^{2+} channel domain (2–4). The cytosolic domain contains all of the key functional sites that confer receptor function and regulation, including an IP_3-binding core (IBC) (15) and an adjacent amino (N)-terminal suppressor domain (SD) (16) that reduces the affinity of IP_3 binding and large regulatory domains responsible for intracellular effector molecules including Ca^{2+} (17). There have been two proposed models for channel gating by IP_3R: direct binding of the IBC/SD domains to the channel domain for gating (18), and long-distance coupling from IBC to the channel, which we proposed in previous structural studies (19, 20). Recent cryo-electron microscopy (cryo-EM) analysis of IP_3R (21, 22) has demonstrated that the IBC is ∼70 Å apart from the Ca^{2+} conducting pore and directly contacts to the C-terminal tail through a long helical bundle connecting to the pore forming the sixth transmembrane helix (S6). How IP_3-binding sites physically communicate with the channel at a long distance remains unknown, however.

An early gel filtration study of overexpressed rat IP_3R1 cytosolic domain detected an IP_3-dependent shift of elution volumes (23), and X-ray crystallography of the IP_3-binding domain provided the first glimpse of IP_3-dependent conformational changes (24). However, the largest IP_3R1 fragment solved to date by X-ray crystallography is limited to the IP_3-binding domain including ∼580 residues in IP_3R1 (24, 25); thus, the major residual part of the receptor containing more than 1,600 residues in the IP_3R cytosolic domain remains unsolved by crystallography, and our understanding of the global conformational changes elicited by IP_3 remains incomplete. In the present study, we performed X-ray crystallography of the cytosolic domain and functional analyses of the IP_3R channel to explore the long-range allosteric mechanism for channel gating.

Results

To unveil the structure of the massive cytosolic domain of the IP_3R constituting 2,217 amino acid residues, we expressed recombinant IP_3R1 truncated with the C-terminal transmembrane domain in insect cells (Fig. 1*A*) using a baculovirus system (19). The size and monodisperse distributions of purified proteins were determined by size exclusion chromatography and dynamic light scattering (DLS) measurements. A truncated construct produced small crystals in an initial screening, but the resolution of diffraction was insufficient, so we constructed various baculoviruses with other truncations or mutations and subsequently

Significance

Cells use chemical signals for intracellular communication in our bodies. Inositol 1,4,5-trisphosphate (IP_3) is a chemical signal that binds to the IP_3 receptor (IP_3R) to release calcium ions from the endoplasmic reticulum. The distance from ligand-binding sites to the channel within IP_3R is the longest among known ligand-gated ion channels, and the fundamental question of how IP_3-binding physically opens the channel remains unanswered. Here, we solved IP_3-bound and unbound structures of large cytosolic domains of the IP_3R by X-ray crystallography and clarified the IP_3-dependent gating mechanism through a unique leaflet structure. These findings reveal a principle of long-range allosteric coupling in ligand-gated ion channels and provide drug targets for IP_3R-regulated events, including autophagy, apoptosis, cancers, and brain disorders.

Author contributions: K.H. and K.M. designed research; K.H., H.M., and A.T. performed research; K.H., A.T., and K.M. contributed new reagents/analytic tools; K.H., H.M., and A.T. analyzed data; and K.H., H.M., and K.M. wrote the paper.

The authors declare no conflict of interest.

This article is a PNAS Direct Submission.

Data deposition: The atomic coordinates and structure factors have been deposited in the Protein Data Bank, www.pdb.org (PDB ID codes 5GUG, 5X9Z, 5XA0, and 5XA1).

[1]To whom correspondence should be addressed. Email: mikosiba@brain.riken.jp.

This article contains supporting information online at www.pnas.org/lookup/suppl/doi:10.1073/pnas.1701420114/-/DCSupplemental.

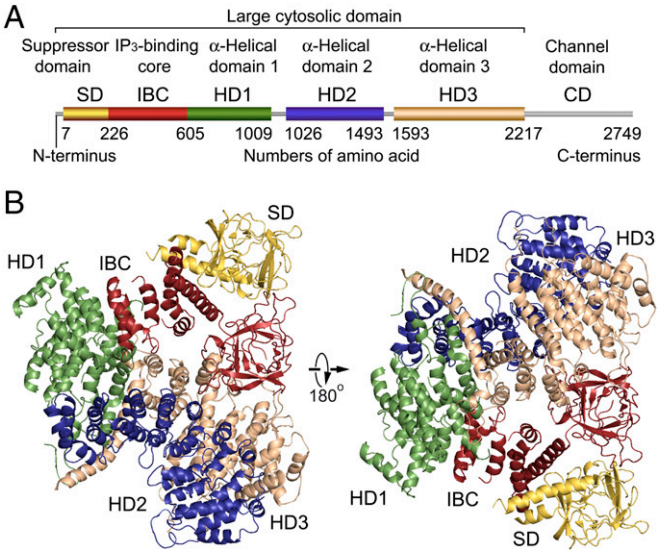

Fig. 1. Global architecture of the IP_3R large cytosolic domain. (*A*) Domain organization. Each domain is depicted in a different color: yellow, suppressor domain (SD; 7–225 amino acid residues); red, IP_3-binding core (IBC; 226–604 residues); green, α-helical domain 1 (HD1; 605–1,009 residues); blue, α-helical domain 2 (HD2; 1,026–1,493 residues); tan, α-helical domain 3 (HD3; residues 1,593–2,217); and gray, channel domain (CD; 2,218–2,749 residues). (*B*) Overall crystal structure of IP_3R2217 viewed from two sides. The overall arrangement of domains is consistent with four crystal structures solved using $C222_1$ and $P4_2$ crystals (5.8–7.4 Å datasets). The left corresponds to a top view from the cytosolic side with respect to the membrane in the tetrameric IP_3R (Fig. S4*F*).

optimized the crystallization conditions. A truncated IP_3R1 including 2,217 residues with an R937G mutation (IP_3R2217) produced diffracting crystals with a rod shape, and another crystal derived from a truncated IP_3R1 including 1,585 residues with an R922G mutation (IP_3R1585) formed bipyramidal crystals (Fig. S1). These rod-shaped and bipyramidal crystals were also grown in the presence of IP_3. For structure determination, the Cα model by cryo-EM (22) did not provide a definitive solution of molecular replacement using any datasets, indicating differences between the crystal structures and the cryo-EM structure; therefore, the divided domains of the cryo-EM model and the published X-ray structures (25) were used as search models, which allowed phasing of the diffraction data of crystals grown under four different conditions, and X-ray structures of the mouse IP_3R1cytosolic domain were obtained using 5.8–7.4 Å datasets (Table S1 and Fig. S2).

The crystal structure of the large cytosolic domain of IP_3R2217 is composed of five domains: an N-terminal SD, IBC, and three curvature α-helical domains 1–3 (HD1–3) (Fig. 1*B*). The distance from the IP_3-binding site, to the edge of HD3 domain was ∼70 Å, consistent with previous reports (19, 22, 26). The α-helices of the C-terminal side of IBC continues to the HD1 domain, and interfaces formed with 737–748 residues of the HD1 domain made a contact with proximal edge of HD2, and another interface consisting of 749–791 residues in the HD1 domain contiguously connected with the N-terminal side of HD3 of 1,593–1,687 residues. The packing of the IP_3R2217 and IP_3R1585 in the crystal showed several contacts between adjacent molecules through each domain in the asymmetric unit (Fig. S2*A*). The overall structure spanning ∼120 Å in diameter is consistent with electron microscopy findings for negatively stained and ice-embedded IP_3R2217 (Fig. S2 *B*–*D*), and similar to a large protruding domain in negative-staining EM observations of tetrameric IP_3R (19, 26). Experimental phasing with heavy atom clusters also support our IP_3R2217 model (Fig. S2 *E*–*F*).

To investigate the effect of IP_3 on global receptor conformation, we solved structures using both IP_3R1585 and IP_3R2217-crystals grown in the absence or presence of IP_3 (Figs. 2 and 3 and Figs. S3 and S4). A comparison of IP_3R1585 structures in the absence and the presence of IP_3 reveals significant changes in the domain arrangements; thus, we measured the rotational angle and shift of HD1 and HD2 in the IP_3R1585 crystal structures (Fig. 2 *A* and *B*). Superposition by fitting two β domains (7–430 residues) shows that the HD1 domain was rotated ∼9° about a P437 residue (8.7° in chain A of two chains in the asymmetry unit, 9.1° in chain B of two chains in the asymmetry unit) and the resultant shift was ∼10 Å (10.0 Å in chain A, 10.4 Å in chain B) as measured by L670 residues. The HD2 domain also rotated 3–4° (3.1° in chain A, 3.9° in chain B), and the shift was ∼5 Å (4.7 Å in chain A, 5.1Å in chain B) as measured by L1449 residues.

To further confirm the IP_3-mediated conformational changes, we compared crystal structures of IP_3R2217 in the absence and presence of IP_3 (Fig. 3 *A* and *B*). Superposition by fitting two β domains (7–430 residues) shows that the HD1 domain rotated ∼7° (7.2° in chain A, 6.8° in chain B) about P437, and the resultant shift was 8–9 Å (8.8 Å in chain A, 8.5 Å in chain B) as measured by L670 residues. The HD3 domain also rotated 3–5° (5.0° in chain A, 3.9° in chain B) about P437, as measured by I1600 residues, and shifted 4–7 Å by IP_3 (6.8 Å in chain A, 4.9 Å in chain B). The HD2 domain rotated 1–2° (2.3° in chain A, 1.4° in chain B) about P437 and shifted 2–3 Å (3.1 Å in chain A, 2.0 Å in chain B) as measured by L1449 residues. The direction of HD1 rotation by IP_3 in the IP_3R2217 was clockwise as viewed from the IP_3-binding site, and this rotation occurred with holding helical arrangements (helices 1–6) within the transitional region between IBC and HD1, in which rotational direction was consistent with that in IP_3R1585 (Fig. 3*C*). The difference around the IP_3-binding site of IP_3R1585 (Fig. 2) from IP_3R2217 (Fig. 3) could be interpreted by domain relocations (Fig. S4*D*) without changes in the core conformation of each structural domain (Fig. S3*D*).

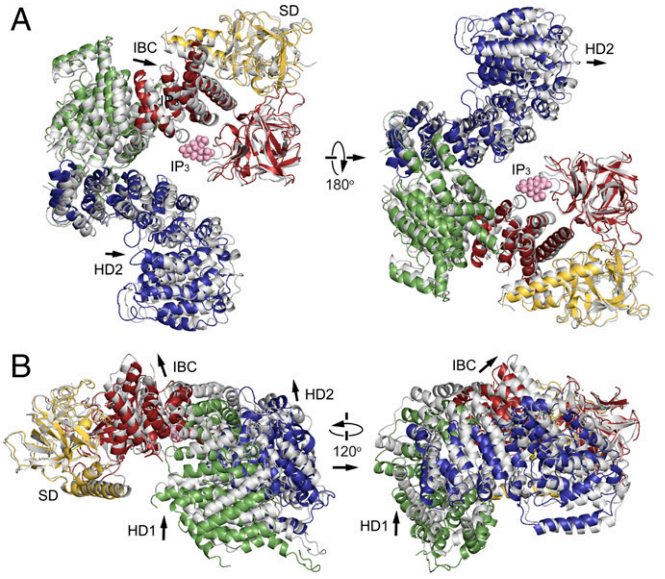

Fig. 2. IP_3-mediated rotation of HD1 about the IP_3-binding site. (*A*) Comparison of IP_3R1585 structures in the absence of IP_3 (colored) with one in the presence of IP_3 (gray). Two structures were superposed by fitting of the N-terminal β-domain (7–430 residues). (*B*) Side views of these two crystal structures. IP_3 molecules are in pink, and arrows indicate the direction of domain relocations by IP_3.

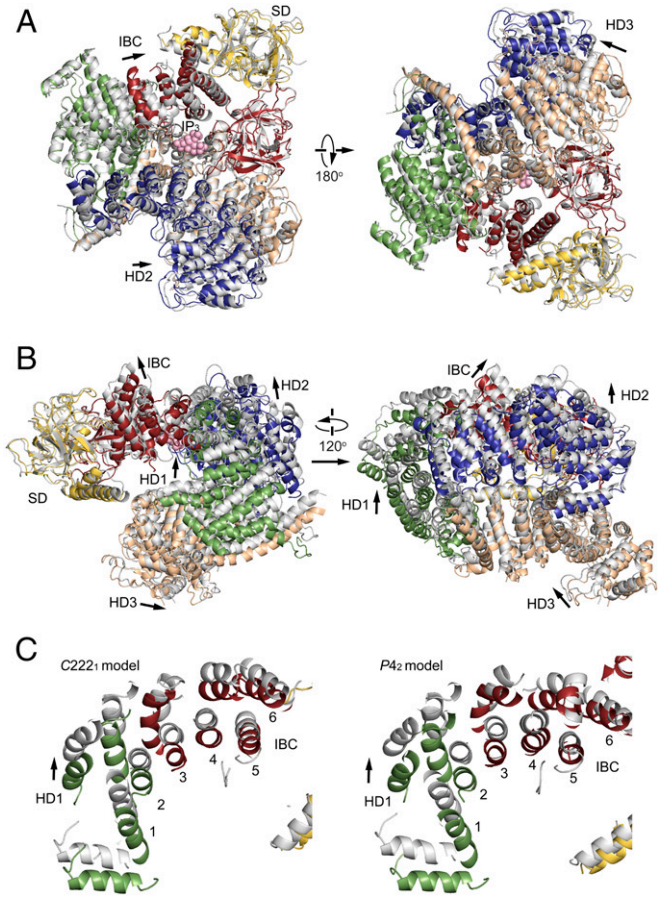

Fig. 3. Long-range conformational changes in the large cytosolic domain by IP_3. (*A*) Comparison of IP_3R2217 structures in the absence of IP_3 (colored) and in the presence of IP_3 (gray). Two structures were superposed by fitting of the N-terminal β-domain (7-430 residues). (*B*) Side views of the two crystal structures. IP_3 molecules are in pink, and arrows indicate the direction of domain relocations by IP_3. (*C*) The helical arrangements (helices 1–6) at transitional regions from IBC to HD1 of IP_3R2217 (*Left*) and IP_3R1585 (*Right*) were viewed from an IP_3-binding site.

To assess an important region for IP_3R function, we estimated interfaces of domains and subunits using our crystal structure and the previous cryo-EM model (22). The subunit interface was formed between SD and IBC, and a critical tyrosine residue (Y167) (27), which is required for IP_3R function but not for IP_3-binding, faced to the interface, suggesting that the subunit interface should be essential for IP_3R function (Fig. S4*F*). The SD also formed subunit interfaces with HD2 and HD3, suggesting that these could have some functional roles as well. The HD3 domain contains an α-helical repeat structure including a putative Ca^{2+} sensor glutamate residue (E2100) (28) located at the loop in a helix–loop–helix fold, consistent with the structure including a conserved glutamate residue (E4032) in the rabbit RyR1 (29, 30). This glutamate residue was located near the interface (Fig. S4*F*), which is formed by the characteristic long helix of SD. However, our previous study showed that deletion of this helix (67–108 residues) had no effect on IP_3R function (27), indicating that this interface contributes a structural rather than functional role, and thus other interfaces should be considered.

To search for a new structural pathway involved in channel gating, we analyzed the Ca^{2+} release activity of full-length mouse IP_3R1 mutants lacking the parts of the HD2 and HD3 domains (HD2-mut: Δ1,268–1,492, and HD3-mut: Δ2,195–2,215) that are most distal from IBC and proximal to the domain/subunit interfaces (Fig. 4*A*), and C-terminal 50 residues that directly bind to IBC unveiled by cryo-EM (CT-mut: Δ2700–2749). The HD2 and HD3 mutant receptors (HD2- and HD3-mut) showed a significant loss of function as judged by a positive and a negative control (Fig. 4 *B* and *C*). This finding is in sharp contrast with the deletion of CT-mut, which showed no decrease but instead a significant increase of IP_3R function at low concentrations of bradykinin (BK) (Fig. 4*C* and Fig. S5*C*). Furthermore, we constructed double mutants (HD2+CT-mut and HD3+CT-mut in Fig. 4*A*) to further examine the functions of these regions. The double mutation with HD2 and CT showed intact IP_3R function, whereas the double mutation with HD3 and CT resulted in complete loss of function (Fig. 4*C*). These results clearly indicate that HD3 is the most essential of these three regions for IP_3R function. Our results also suggest that HD2 and CT have regulatory roles, but not essential roles, in line with previous data for a mutant lacking 249 residues in HD2 of mouse IP_3R1 (31) or a mutant lacking 33 residues in CT of rat IP_3R1 (32). These domains likely can facilitate isoform-specific regulation because of the low sequence homology in these areas among IP_3R isoforms.

To verify our findings for the HD3 domain, we constructed six kinds of glycine substitution mutants (Fig. 5 *A* and *B* and Fig. S6). First, we divided the leaflet structure from 2,195–2,215 amino acid residues into the two parts (2,195–2,294 and 2,295–2,215 residues) and constructed 10 glycine substitutions (10G-mut) and 11 glycine substitutions (11G-mut) and examined their function. Both 10G-mut and 11G-mut activities were disrupted, confirming our conclusion that this leaflet structure is required for IP_3R function (Fig. 5*C*). Next, we further divided the leaflet

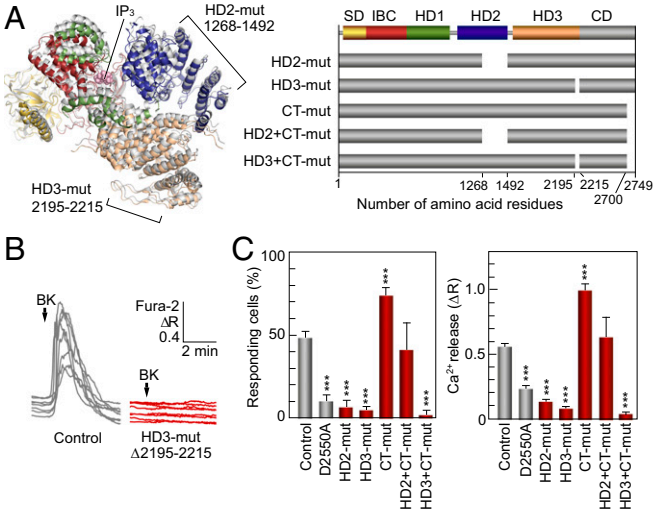

Fig. 4. Essential role of HD3 on IP_3R channel gating. (*A*) Two regions deleted in mutants lacking1,268-1,492 residues in HD2 domain and 2,195–2,215 residues in HD3 domain are depicted in the IP_3R2217 crystal structure (*Left*), and our prepared deletion mutants are schematized (*Right*). (*B*) The 0.3-nM BK-evoked Ca^{2+} release from the ER was measured in Neuro2a cells under a nominally Ca^{2+}-free condition. Typical responses of eight cells transfected with full length IP_3R1 (control) or with HD3-mut (Δ2195–2215) were presented in the differences of Fura-2 ratio. (*C*) Bar charts summarizing the relative population ± SEM (%) of 0.3 nM BK responding cells calculated from data of more than four independent experiments (*Left*) and the amplitude of $[Ca^{2+}]i$ increase ± SEM (ΔR) calculated from data of more than 30 cells in (*Right*) (control, $n = 326$; D2550A, $n = 183$; HD2-mut, $n = 121$; HD3-mut, $n = 228$; CT-mut, $n = 244$; HD2+CT-mut, $n = 35$; HD3+CT-mut, $n = 96$). A Ca^{2+}-conducting pore mutant (D2550A) served as a negative control (50). The significance of multiple comparisons was estimated by Dunnett's method. $***P < 1 \times 10^{-5}$.

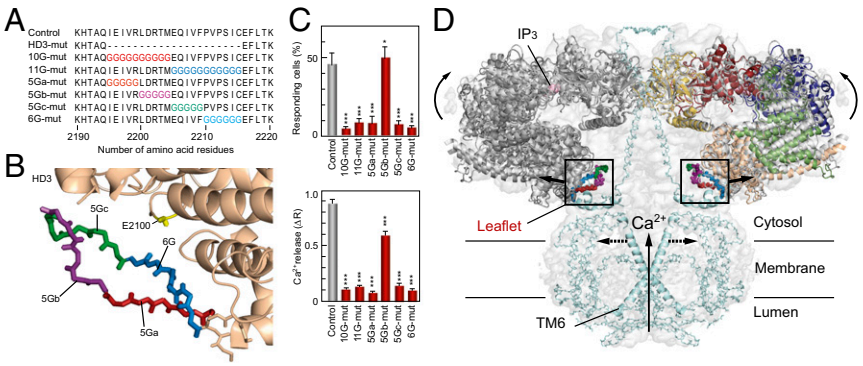

Fig. 5. Critical sites in HD3 responsible for channel gating. (*A*) Amino acid sequences represent our mutated sites in which 10–11 amino acid residues (10G- and 11G-mut) or 5–6 amino acid residues (5Ga-, 5Gb-, 5Gc-, and 6G-mut) were substituted for glycine residues. (*B*) Mutated sites in the IP_3R2217 crystal structure: 5Ga-mut, red; 5Gb-mut, purple; 5Gc-mut, green; and 6G-mut, blue. A critical glutamate residue, E2100, is shown in yellow. (*C*) Bar charts summarizing the relative population ± SEM (%) of 0.3 nM BK responding cells calculated from data of more than seven independent experiments (*Left*) and the amplitude of $[Ca^{2+}]i$ increase ± SEM (ΔR) calculated from data of more than 50 cells (*Right*) (control, $n = 167$; D2550A, $n = 58$; 10G-mut, $n = 137$; 11G-mut, $n = 90$; 5Ga-mut, $n = 171$; 5Gb-mut, $n = 144$; 5Gc-mut, $n = 163$; 6G-mut, $n = 149$). The significance of multiple comparisons was estimated by Dunnett's method. $*P = 0.0139$; $***P < 0.001$. (*D*) Model for IP_3-dependent gating mechanism of IP_3R. Two opposing IP_3R2217 molecules are delineated by superimposing in the cryo-EM map (EMD-6369). Color codes of domains and critical sites in the leaflet structure are the same as in Figs. 1 and 3. The Ca^{2+} conducting pore formed with the transmembrane helix and the C-terminal region (light blue) were prepared according to coordinates of rat IP_3R1 (PDB ID code 3JAV). We propose that IP_3-dependent global conformational changes and gating transmission by the leaflet structure work in concert to open the channel pore (dotted lines).

into five or six amino acid residues and constructed four glycine substitution mutants (Fig. 5 *A* and *B*). The IP_3R activities of three of these mutants (5Ga-, 5Gc-, and 6G-mut) were significantly reduced, and only 5Gb-mut retained IP_3R function (Fig. 5*C*). These data indicate two discontinuous sections, consisting of 2,195–2,199 residues and 2,205–2,215 residues, which are essential for IP_3R function.

Discussion

The mechanism of how IP_3 opens the Ca^{2+} channel in the IP_3R has remained elusive because of difficulties associated with the long distance between IP_3-binding sites and the Ca^{2+} channel. Our present study reveals long-range conformation changes of the IP_3R cytosolic domain from the IP_3-binding site to the channel domain, consisting of more than 2,000 amino acid residues, in response to IP_3, and also clarifies that IP_3R function requires a small leaflet structure containing only 21 amino acid residues, located at the most distal location of the IP_3-binding site. Therefore, we conclude that an IP_3-dependent conformation change is transmitted from IBC to the channel through HD1 and HD3 containing the leaflet region (Fig. 5*D*). Mutation analyses of the leaflet region have unveiled essential roles not only of residues facing the cytosolic domain, but also of residues facing the channel domain; thus, the double-edged sides of the leaflet are involved in relaying IP_3-dependent conformational status from the large cytosolic domain to the channel pore.

Our study is a crystallographic analysis demonstrating that a local IP_3-binding event by several amino acid residues coordinating with IP_3 molecule spreads to the entire large cytosolic architecture. The most conspicuous conformational change was caused by relocation of HD1 with respect to the N-terminal β-domains in both IP_3R2217 and IP_3R1585 crystals, and it is notable that this domain rotated about a transition point from the β-structure to the α-structure in the IBC. Furthermore, this rotation about the pivot point determines the position of the HD3 domain that connects to the Ca^{2+} channel domain. In SD/IBC domains, the α-helical region of IBC slightly moves closer to the β-domains by anticlockwise rotation as viewed from the top, and it rotates toward the top along a vertical axis in a clockwise direction as viewed from the IP_3-binding site, in line with previous studies about the SD/IBC domains (24, 25). These two directions reflect the horizontal and vertical movement of HD1 in IP_3R2217 and IP_3R1585 (Figs. 2 and 3), which should affect HD3 relocation along the horizontal direction in which HD3 domains become more distal from the fourfold axis in the tetrameric IP_3R (Fig. 5*D*). Consequently, the motion of leaflet region could shift the pore-forming TM6 helix to open the Ca^{2+} pore (dotted line in Fig. 5*D*).

In the tetrameric IP_3R1, the globular β-domain of SD interacts with the β-domain of IBC of a neighboring subunit through the Y167-containing interface (Fig. S4*F*), which constructs the ring arrangement eight globular β-domains at the top of the IP_3R (22, 25), consistent with the RyR (29, 33–35). We suggest that this β-domain ring serves as a fixed end of the large cytosolic domain to enable efficient gating transmission from IP_3 to the channel. The reason why Y167 mutation can disrupt IP_3R function despite its long distance from the channel may be elucidated by the instability of the β-domain ring and the resulting inaccuracy of gating transmission. Fan et al. (22) proposed that the channel activation by IP_3 would occur by the direct coupling of the C terminus with IBC (N-C coupling) and by the coupling of SD to an armadillo repeat domain 3 (ARM3)/intervening lateral domain (ILD) of neighboring subunits (SD-ARM3-ILD). Our present functional data support the SD-ARM3-ILD pathway rather than N-C coupling; however, the SD long helix (67–108 residues) contacting with ARM3 is not essential for IP_3R function, as revealed by our previous study (27). Therefore, we propose a new pathway from IBC to the leaflet/ILD regions through the HD1 and HD3 domains (IBC-HD1-HD3-leaflet). This pathway is structurally supported by IP_3-dependent conformational changes (Fig. 5*D*). Our structural comparison with crystal structures and the cryo-EM structure revealed two aspects within the subunit conformation: an immobile arrangement of curvature helical structure consisting of the HD1 and HD3 domains, consistent with the cryo-EM model (Fig. S4*E*), and variable arrangements of HD2 in relation to HD1, shown by the large difference between our crystal structures and the cryo-EM structure (Fig. S4 *A*–*D*), and variable placements of IBC relative to HD1, shown by the difference between IP_3R1585 and IP_3R2217 (Fig. S4 *A*, *C*, and *D*). During IP_3-dependent channel activation, the former architecture would act as a rigid body conducting a torque from IP_3-binding sites to the channel domain, whereas the flexible regions would contribute to the dynamic properties of the IP_3R. Despite the *apo* state of IP_3R, the spatial relationship between IBC and HD1 was

found to be variable; interestingly, this area contains a pivotal locus responsible for IP_3-binding. Therefore, the dynamic nature around the IP_3-binding site provides a plausible conformational landscape for ligand-dependent conformational selection.

The sequence alignment of IP_3R and RyR indicates that the equivalent leaflet region in the RyR intervenes to the Ca^{2+}- and Zn^{2+}-binding sites in the 3D structure revealed by a recently reported cryo-EM study (36) (Fig. S6 *D* and *E*), suggesting integrative roles of this region underlying channel activation. Considering that the RyR Ca^{2+}-binding pocket is common with IP_3R (36), and that Ca^{2+} regulates IP_3R (17) in a similar manner to RyR, the contact of the leaflet to the Ca^{2+}-binding site suggests Ca^{2+}-dependent activation of leaflet-mediated gating transmission and/or leaflet-mediated activation of Ca^{2+} binding. The functional role of Zn^{2+} ions in IP_3R remains largely unknown, but our previous mutagenesis study demonstrated a complete loss of IP_3R function with a C2610 or a C2613 mutation (31), corresponding to the zinc-finger motif of RyR2 (37); thus, the intervening leaflet presumably can mediate structural and functional coupling between the Ca^{2+}- and Zn^{2+}-binding sites. In particular, here we found that the 5Ga region, but not the 5Gb region, closely faces the helix bridging between these sites and contains highly conserved isoleucine (I2195), glutamate (E2196), and isoleucine (I2197) residues in IP_3R of all isoforms and various animals (Fig. S6 *D* and *E*). Thus, these residues are candidates for mediating gating transmission to the channel domain. The deletion of the leaflet-containing region had no effect on IP_3-binding affinity and cooperativity (31), thus the IP_3-dependent conformational change should occur independently of the mutations within the leaflet. Therefore, the reason for defects in the IP_3-mediated motion of TM6 helices in the mutants is that the leaflets of 5Ga and 5Gc/6G mutants could not physically connect with the helix bridging between the Ca^{2+}- and Zn^{2+}-binding sites and the helix in HD3, respectively. To our knowledge, this mechanistic insight is our original model of IP_3-dependent long-range communication from the IP_3-binding site to the channel through the large helical architecture including HD1, HD3, and the leaflet, providing strategies for further study and drug development of the IP_3R.

Methods

Expression and Purification of IP_3R1585 and IP_3R2217. All baculoviruses were amplified in *Spodoptera frugiperda* (Sf-9) insect cell lines, harvested, and infected into insect cells for expression as described previously (19), following the manufacturer's protocol (Life Technologies). Insect cells were incubated at 27 °C for 2 d after being infected with IP_3R1585- or IP_3R2217-encoding baculoviruses and then harvested by centrifugation at 1,500 rpm in a table-top centrifuge (model 8420; Kubota), washed with 3 volumes of ice-cold PBS at least twice, frozen in liquid nitrogen, and stored at −80 °C in a Revco freezer (Thermo Fisher Scientific). The IP_3R1585 and IP_3R2217 proteins were purified as described previously (19, 38), with modifications. Baculovirus preparation and protein purification are described in more detail in *SI Methods*.

Crystallization and Data Collection. Screening of crystallization conditions was performed with the CrystalPro protein crystal imaging system (TriTek). Initial crystals were obtained by 96-well sitting drop screens using several lines of screening kits (Qiagen). The first crystals of IP_3R1585 and IP_3R2217 obtained were ∼10 μm in size and had rice-like and rod-like shapes, respectively. For diffraction experiments, IP_3R1585 was diluted with 10 mM Hepes buffer (pH 7.3) containing 150 mM NaCl, 1 mM TCEP, and 0.3 mM IP_3 (or without IP_3), and crystallization was carried out at 18 °C in hanging drops consisting of 1.5 μL of protein solution (20 mg/mL) and 1.5 μL of reservoir solution. Crystals appeared in the tetragonal space group $P4_2$ with two molecules of IP_3R1585 in the asymmetric unit. The crystals were grown in lithium sulfate concentrations ranging from 1.45 to 1.8 M in 0.1 M Hepes buffer (pH 7.1–7.5). Crystals reached full size in 2 wk, at which point they were picked with a cryo loop, cryoprotected by increasing glycerol concentrations, and flash-frozen in a liquid nitrogen stream at 100 K. Crystals of IP_3R2217 appeared in the orthorhombic space group $C222_1$ with two molecules of IP_3R2217 in the asymmetric unit. Cryoprotectants for IP_3R2217 crystals were screened using CryoPro (Hampton Research), and glycerol was chosen as a suitable cryoprotectant. The crystals used for diffraction experiments were obtained from 7.5 mg/mL IP_3R2217 and grown using sodium citrate as a precipitant at concentrations ranging from 0.5 to 0.7 M in 100 mM imidazole buffer (pH 6.9–8) and 12% (vol/vol) glycerol in the absence and presence of 0.1 mM IP_3. Crystals reached full size in 1–4 wk at 22 °C, at which time they were picked with a cryo loop and flash-frozen in a liquid nitrogen stream at 100 K without additional cryoprotectant. Heavy atom derivatives were obtained by soaking crystals in precipitant solutions containing several heavy atoms using Heavy Atom Screens (Hampton Research) and Phasing Kits (Jena Bioscience), and the stability of crystals was evaluated by X-ray diffraction. Full datasets of IP_3R2217 crystals soaked in solutions containing 1 mM tantalum bromide clusters (Ta_6Br_{12}) and 1 mM tungsten clusters ($PW_{12}O_{40}$ and $H_2W_{12}O_{40}$) could be collected. Diffraction data were collected using a Mar225 CCD detector at the BL26B1/B2 stations in the RIKEN SPring-8 facility using a mail-in data collection system (39, 40).

Crystal quality was checked by measuring diffraction using a Rayonix MX226HE CCD detector at RIKEN SPring-8 station BL32XU. X-ray diffraction data were obtained from crystals of IP_3R2217 (0.19 mm × 0.038 mm), IP_3R1585 (0.34 mm × 0.14 mm), and IP_3R1585 with IP_3 (0.27 mm × 0.1 mm) using a 1.0-Å wavelength, and were processed using HKL2000 (41) and XDS (42). Exposure times were 20, 30, and 25 s/frame for IP_3R2217, IP_3R1585, and IP_3R1585 with IP_3, respectively, and the oscillation range was 1.0°.

Structure Determination of the Large Cytosolic Domain. To prepare a search model for molecular replacement, a polyalanine model of the regulatory domain (585–2,217 amino acids) was built on Cα models of rat IP_3R1 (3JAV) (22) using Coot (43). No definitive solution was obtained for either crystal form, however; thus, we divided the polyalanine model into four domains and searched for them or previously solved crystal structures by molecular replacement with the Phaser program (44) in the Phenix suite version 1.9, and obtained definitive solutions for two IBDs (25) and five regulatory domains in the asymmetric unit of the $C222_1$ crystal lattice (Fig. S1*B*). In each step of molecular replacement, numerous rod-shaped electron densities appeared outside the model in which residual models were precisely placed after additional molecular replacements (Fig. S1*C*), indicating that the models were correctly placed. After placing seven domains, the resulting map also showed clear electron density in the Fo-Fc map, which allowed placing of the eighth domain. No domains ever clashed with neighboring domains (Fig. S2*A*), and the contiguous chain traces between domains as well as the electron density maps support the correct locations of the domains. Electron microscopy observation of IP_3R2217 and its class average calculated with an EMAN2 program (45) also supported the size and shape of the large cytosolic domain determined by crystallographic analyses (Fig. S2 *B*–*D*).

To confirm our model built by molecular replacement, we performed experimental phasing (Fig. S2 *E* and *F*) as described in *SI Methods*. The crystallographic refinements (Table S1) were carried out using the phenix.refine program (46) in the Phenix 1.10 software package (47). This experiment is described in detail in *SI Methods*.

Ca^{2+} Imaging. Neuro2a cells (American Type Culture Collection; CCL-131) were seeded in 3.5-cm glass-bottom dishes and cultivated for 1 d in 2 mL of DMEM containing 10% (vol/vol) FBS, 100 U/mL penicillin, and 100 μg/mL streptomycin, and then transfected with plasmids for wild-type or mutant full-length IP_3R using FuGENE (Promega) as described previously (14, 48, 49). At 1 d after transfection, Fura 2-AM was loaded into Neuro2a cells by incubation with 5 μM Fura 2-AM in balanced salt solution containing 115 mM NaCl, 5.4 mM KCl, 2 mM $CaCl_2$, 1 mM $MgCl_2$, 20 mM Hepes, pH 7.4, and 10 mM glucose for 30 min at room temperature. Then Ca^{2+} imaging was performed using an inverted fluorescence microscope with a 20× objective lens (S Fluor 20×, NA 0.75; Nikon) and AQUACOSMOS (Hamamatsu Photonics) to obtain F340/F380 ratio images as described previously (14, 48, 49). To monitor Ca^{2+} release from the ER, Neuro2a cells were perfused with Ca^{2+}-free BSS for 2 min immediately before $[Ca^{2+}]i$ measurements.

Recombinant IP_3R1, which was expressed as an EGFP-fusion protein, was prepared using several primers (Figs. S5 and S6). The HD3-mut (Δ2,195–2,215) was constructed by replacing a PCR product amplified with P1 and P2 primers into the BamHI and EcoRI sites of pcDNA3.1/Zeo(+)/EGFP-IP_3R1 (Fig. S5). The HD2-mut (Δ1,268–1,492) and CT-mut (Δ2,700–2,749) mutants were constructed by inserting a PCR product amplified with P3/P4 and P5/P6 primers into pcDNA3.1/Zeo(+)/EGFP-IP_3R1 through the BamHI/BamHI and SbfI/XhoI sites, respectively (Fig. S5). Double mutants (HD2+CT- and HD3+CT-mut) were constructed by combining two mutants. All substitution mutants (10G-, 11G-, 5Ga-, 5Gb-, 5Gc-, and 6G-mut) were constructed by replacing PCR products amplified with P7–P12 primers into the BamHI and EcoRI sites of pcDNA3.1/Zeo(+)/EGFP-IP_3R1 (Fig. S6).The pore mutant D2550A (50) was

BIOCHEMISTRY

prepared using the Stratagene QuikChange Kit and used as a negative control. The deletion and point mutations were confirmed by sequence analysis using an ABI 3730xl automatic sequencer (Applied Biosystems). Expression of the full-length IP_3R1 was confirmed by Western blot analysis and by the fluorescence of GFP in the living cells (Fig. S5 *B* and *D*). Also confirmed were the targeting and distribution of these mutants in the ER (Fig. S5*E*) and glycosylation using ConA-Sepharose (Fig. S5*F*). $[Ca^{2+}]i$ was measured in GFP^+ Neuro2a cells stimulated with 0.3 nM (Figs. 4 and 5 and Fig. S6*C*) or 1 nM BK (Fig. S5*C*) under nominally Ca^{2+}-free conditions to evaluate Ca^{2+} release from the ER through the recombinant IP_3R1. The functions of the R922G and R937G mutants were confirmed by plasmids constructed with the mutated fragment and pcDNA3.1/Zeo(+)/EGFP-IP_3R1 (Fig. S6 *B* and *C*).

ACKNOWLEDGMENTS. We thank Drs. Yuki Nakamura, Go Ueno, and Masaki Yamamoto for the X-ray diffraction data measurements using the mail-in data collection system at RIKEN SPring-8; Dr. Kyoko Nakamura (Juntendo University) for Ca^{2+} measurements; Dr. Charles Yokoyama (RIKEN) for editing the manuscript; Kazu Hoshi (JEOL) for performing cryo-EM; and the RIKEN Research Resources Center for the Tecnai12 electron microscope. This study was supported by the Japan Society for the Promotion of Science through Grant-in-Aid for Scientific Research C (Grant 15K06791, to K.H.), Innovative Areas (Brain Protein Aging and Dementia Control) (Grant 15H01572, to K.H.), Encouragement of Scientists (Grant 24926012, to A.T.), Scientific Research S (Grant 25221002, to K.M.), the Japan Science and Technology Agency's International Cooperative Research Project–Solution-Oriented Research for Science and Technology (K.M.), and a RIKEN Brain Science Institute Grant and President's Fund (to K.M.). Supercomputing resources were provided by the Human Genome Center at Tokyo University and by the Advanced Center for Computing and Communication at RIKEN. Cryo-EM was supported by the Nanotechnology Platform (Project 12024046).

1. Berridge MJ (1993) Inositol trisphosphate and calcium signalling. *Nature* 361:315–325.
2. Mikoshiba K (2007) IP3 receptor/$Ca2^+$ channel: From discovery to new signaling concepts. *J Neurochem* 102:1426–1446.
3. Patterson RL, Boehning D, Snyder SH (2004) Inositol 1,4,5-trisphosphate receptors as signal integrators. *Annu Rev Biochem* 73:437–465.
4. Furuichi T, et al. (1989) Primary structure and functional expression of the inositol 1,4,5-trisphosphate-binding protein P400. *Nature* 342:32–38.
5. Nishiyama M, Hong K, Mikoshiba K, Poo MM, Kato K (2000) Calcium stores regulate the polarity and input specificity of synaptic modification. *Nature* 408:584–588.
6. Harnett MT, Bernier BE, Ahn KC, Morikawa H (2009) Burst-timing-dependent plasticity of NMDA receptor-mediated transmission in midbrain dopamine neurons. *Neuron* 62:826–838.
7. Fujii S, Matsumoto M, Igarashi K, Kato H, Mikoshiba K (2000) Synaptic plasticity in hippocampal CA1 neurons of mice lacking type 1 inositol-1,4,5-trisphosphate receptors. *Learn Mem* 7:312–320.
8. Sugawara T, et al. (2013) Type 1 inositol trisphosphate receptor regulates cerebellar circuits by maintaining the spine morphology of Purkinje cells in adult mice. *J Neurosci* 33:12186–12196.
9. Di Gregorio E, et al. (2010) Two Italian families with ITPR1 gene deletion presenting a broader phenotype of SCA15. *Cerebellum* 9:115–23.
10. Hara K, et al. (2008) Total deletion and a missense mutation of ITPR1 in Japanese SCA15 families. *Neurology* 71:547–551.
11. Cheung KH, et al. (2008) Mechanism of $Ca2^+$ disruption in Alzheimer's disease by presenilin regulation of InsP3 receptor channel gating. *Neuron* 58:871–883.
12. Mattson MP (2004) Pathways towards and away from Alzheimer's disease. *Nature* 430:631–639.
13. Tang TS, et al. (2003) Huntingtin and Huntingtin-associated protein 1 influence neuronal calcium signaling mediated by inositol-(1,4,5) triphosphate receptor type 1. *Neuron* 39:227–239.
14. Higo T, et al. (2010) Mechanism of ER stress-induced brain damage by IP(3) receptor. *Neuron* 68:865–878.
15. Yoshikawa F, et al. (1996) Mutational analysis of the ligand binding site of the inositol 1,4,5-trisphosphate receptor. *J Biol Chem* 271:18277–18284.
16. Yoshikawa F, Iwasaki H, Michikawa T, Furuichi T, Mikoshiba K (1999) Cooperative formation of the ligand-binding site of the inositol 1,4, 5-trisphosphate receptor by two separable domains. *J Biol Chem* 274:328–334.
17. Finch EA, Turner TJ, Goldin SM (1991) Calcium as a coagonist of inositol 1,4,5-trisphosphate-induced calcium release. *Science* 252:443–446.
18. Boehning D, Joseph SK (2000) Direct association of ligand-binding and pore domains in homo- and heterotetrameric inositol 1,4,5-trisphosphate receptors. *EMBO J* 19: 5450–5459.
19. Hamada K, Terauchi A, Mikoshiba K (2003) Three-dimensional rearrangements within inositol 1,4,5-trisphosphate receptor by calcium. *J Biol Chem* 278:52881–52889.
20. Hamada K, Mikoshiba K (2012) Revisiting channel allostery: A coherent mechanism in IP_3 and ryanodine receptors. *Sci Signal* 5:pe24.
21. Ludtke SJ, et al. (2011) Flexible architecture of IP3R1 by cryo-EM. *Structure* 19: 1192–1199.
22. Fan G, et al. (2015) Gating machinery of $InsP_3R$ channels revealed by electron cryomicroscopy. *Nature* 527:336–341.
23. Mignery GA, Südhof TC (1990) The ligand binding site and transduction mechanism in the inositol-1,4,5-triphosphate receptor. *EMBO J* 9:3893–3898.
24. Lin CC, Baek K, Lu Z (2011) Apo and $InsP_3$-bound crystal structures of the ligand-binding domain of an $InsP_3$ receptor. *Nat Struct Mol Biol* 18:1172–1174.
25. Seo MD, et al. (2012) Structural and functional conservation of key domains in $InsP_3$ and ryanodine receptors. *Nature* 483:108–112.
26. Hamada K, Miyata T, Mayanagi K, Hirota J, Mikoshiba K (2002) Two-state conformational changes in inositol 1,4,5-trisphosphate receptor regulated by calcium. *J Biol Chem* 277:21115–21118.
27. Yamazaki H, Chan J, Ikura M, Michikawa T, Mikoshiba K (2010) Tyr-167/Trp-168 in type 1/3 inositol 1,4,5-trisphosphate receptor mediates functional coupling between ligand binding and channel opening. *J Biol Chem* 285:36081–36091.
28. Miyakawa T, et al. (2001) Ca(2+)-sensor region of IP(3) receptor controls intracellular Ca(2+) signaling. *EMBO J* 20:1674–1680.
29. Yan Z, et al. (2015) Structure of the rabbit ryanodine receptor RyR1 at near-atomic resolution. *Nature* 517:50–55.
30. Chen SR, Ebisawa K, Li X, Zhang L (1998) Molecular identification of the ryanodine receptor $Ca2^+$ sensor. *J Biol Chem* 273:14675–14678.
31. Uchida K, Miyauchi H, Furuichi T, Michikawa T, Mikoshiba K (2003) Critical regions for activation gating of the inositol 1,4,5-trisphosphate receptor. *J Biol Chem* 278: 16551–16560.
32. Schug ZT, Joseph SK (2006) The role of the S4-S5 linker and C-terminal tail in inositol 1,4,5-trisphosphate receptor function. *J Biol Chem* 281:24431–24440.
33. Efremov RG, Leitner A, Aebersold R, Raunser S (2015) Architecture and conformational switch mechanism of the ryanodine receptor. *Nature* 517:39–43.
34. Zalk R, et al. (2015) Structure of a mammalian ryanodine receptor. *Nature* 517:44–49.
35. Tung CC, Lobo PA, Kimlicka L, Van Petegem F (2010) The amino-terminal disease hotspot of ryanodine receptors forms a cytoplasmic vestibule. *Nature* 468:585–588.
36. des Georges A, et al. (2016) Structural basis for gating and activation of RyR1. *Cell* 167:145–157 e117.
37. Peng W, et al. (2016) Structural basis for the gating mechanism of the type 2 ryanodine receptor RyR2. *Science* 354:aah5324.
38. Maeda N, Niinobe M, Mikoshiba K (1990) A cerebellar Purkinje cell marker P400 protein is an inositol 1,4,5-trisphosphate ($InsP_3$) receptor protein: Purification and characterization of $InsP_3$ receptor complex. *EMBO J* 9:61–67.
39. Ueno G, et al. (2006) RIKEN structural genomics beamlines at the SPring-8: High-throughput protein crystallography with automated beamline operation. *J Struct Funct Genomics* 7:15–22.
40. Okazaki N, et al. (2008) Mail-in data collection at SPring-8 protein crystallography beamlines. *J Synchrotron Radiat* 15:288–291.
41. Otwinowski Z, Minor W (1997) Processing of X-ray diffraction data collected in oscillation mode. *Methods Enzymol Macromol Crystallogr A* 276:307–326.
42. Kabsch W (2010) XDS. *Acta Crystallogr D Biol Crystallogr* 66:125–132.
43. Emsley P, Lohkamp B, Scott WG, Cowtan K (2010) Features and development of Coot. *Acta Crystallogr D Biol Crystallogr* 66:486–501.
44. McCoy AJ (2007) Solving structures of protein complexes by molecular replacement with Phaser. *Acta Crystallogr D Biol Crystallogr* 63:32–41.
45. Tang G, et al. (2007) EMAN2: An extensible image processing suite for electron microscopy. *J Struct Biol* 157:38–46.
46. Afonine PV, et al. (2012) Towards automated crystallographic structure refinement with phenix.refine. *Acta Crystallogr D Biol Crystallogr* 68:352–367.
47. Adams PD, et al. (2010) PHENIX: A comprehensive Python-based system for macromolecular structure solution. *Acta Crystallogr D Biol Crystallogr* 66:213–221.
48. Hamada K, et al. (2014) Aberrant calcium signaling by transglutaminase-mediated posttranslational modification of inositol 1,4,5-trisphosphate receptors. *Proc Natl Acad Sci USA* 111:E3966–E3975.
49. Nakamura K, et al. (2013) Distinct roles of M1 and M3 muscarinic acetylcholine receptors controlling oscillatory and non-oscillatory $[Ca^{2+}]i$ increase. *Cell Calcium* 54: 111–119.
50. Boehning D, Mak DO, Foskett JK, Joseph SK (2001) Molecular determinants of ion permeation and selectivity in inositol 1,4,5-trisphosphate receptor $Ca2^+$ channels. *J Biol Chem* 276:13509–13512.